

# Cyclic Control of the Surface Properties of a Monolayer-Functionalized Electrode by the Electrochemical Generation of Hg Nanoclusters

Michael Riskin, Bernhard Basnar, Eugenio Katz, and Itamar Willner\*<sup>[a]</sup>

**Abstract:** Hg<sup>2+</sup> ions are bound to a 1,4-benzenedimethanethiol (BDMT) monolayer assembled on a Au electrode. Electrochemical reduction of the Hg<sup>2+</sup>-BDMT monolayer to Hg<sup>+</sup>-BDMT (at  $E^\circ=0.48$  V) and subsequently to Hg<sup>0</sup>-BDMT (at  $E^\circ=0.2$  V) proceeds with electron-transfer rate constants of 8 and 11 s<sup>-1</sup>, respectively. The Hg<sup>0</sup> atoms cluster into aggregates that exhibit dimensions of 30 nm to 2  $\mu$ m, within a time interval of minutes. Electrochemical oxidation of the nanoclusters to Hg<sup>+</sup> and further oxidation to Hg<sup>2+</sup> ions proceeds with electron-transfer rate constants corresponding to 9 and 43 s<sup>-1</sup>, respectively, and the re-

distribution of Hg<sup>2+</sup> on the thiolated monolayer occurs within approximately 15 s. The reduction of the Hg<sup>2+</sup> ions to the Hg<sup>0</sup> nanoclusters and their reverse electrochemical oxidation proceed without the dissolution of mercury species to the electrolyte, implying high affinities of Hg<sup>2+</sup>, Hg<sup>+</sup>, and Hg<sup>0</sup> to the thiolated monolayer. The electrochemical transformation of the Hg<sup>2+</sup>-thiolated monolayer to the Hg<sup>0</sup>-nanocluster-

functionalized monolayer is characterized by electrochemical means, surface plasmon resonance (SPR), X-ray photoelectron spectroscopy (XPS), scanning electron microscopy (SEM), atomic force microscopy (AFM), and contact-angle measurements. The Hg<sup>0</sup>-nanocluster-modified surface reveals enhanced hydrophobicity (contact angle 76°) as compared to the Hg<sup>2+</sup>-thiolated monolayer (contact angle 57°). The hydrophobic properties of the Hg<sup>0</sup>-nanocluster-modified electrode are further supported by force measurements employing a hydrophobically modified AFM tip.

**Keywords:** electrochemistry • mercury • monolayers • nanoclusters • nanostructures • surface plasmon resonance

## Introduction

The control of the hydrophilic and hydrophobic properties of surfaces attracts substantial research efforts, and the generation of superhydrophobic surfaces has important practical applications.<sup>[1]</sup> Monolayer-functionalized surfaces,<sup>[2]</sup> and organic<sup>[3]</sup> or inorganic<sup>[4]</sup> polymers organized as thin-films on supports have been used to control the hydrophilic and hydrophobic properties of the interfaces. Thermal or pH triggers have been used to switch the superhydrophobic and superhydrophilic properties of surfaces modified with poly-[(isopropyl acrylamide)-co-(acrylic acid)] copolymer.<sup>[5]</sup> Electrochemical,<sup>[6]</sup> photochemical,<sup>[7]</sup> magnetic,<sup>[8]</sup> chemical,<sup>[9]</sup> or

biocatalytic<sup>[10]</sup> stimuli have been used to control the hydrophilic–hydrophobic properties of surfaces. For example, the electrical-field-induced bending of the negatively charged carboxylate unit tethered to a long alkyl chain on an electrode was used to control the hydrophilic–hydrophobic properties of a Au surface.<sup>[11]</sup> Similarly, the electrochemically driven transport of a charged “molecular shuttle” on a molecular-wire supramolecular structure, in a monolayer configuration, was used to switch the hydrophilic–hydrophobic properties of the electrode surface.<sup>[12]</sup> Photochemical control of the surface properties of semiconductor-functionalized supports by photoinduced redox transformation of surface groups has been reported. Similarly, photoisomerization of photochromic molecules in monolayer structures has been extensively used to control the hydrophilic–hydrophobic properties of surfaces.<sup>[13]</sup> Chemical stimuli, such as pH, have been applied to control the properties of surfaces.<sup>[14]</sup> Several studies have addressed the wetting properties of surfaces modified with nanoparticles.<sup>[15]</sup> Superhydrophobic behavior of the lotus-leaf structure has been discovered for the nanoparticle-functionalized interfaces, thus demonstrating the significant effect of nanoparticles on the wettability

[a] M. Riskin, Dr. B. Basnar, Dr. E. Katz, Prof. I. Willner  
Institute of Chemistry  
and The Center for Nanoscience and Nanotechnology  
The Hebrew University of Jerusalem, Jerusalem 91904 (Israel)  
Fax: (+972)2-652-7715  
E-mail: willnea@vms.huji.ac.il

Supporting information for this article is available on the WWW under <http://www.chemeurj.org/> or from the author.

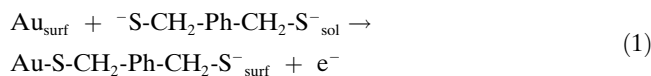
properties of the modified surfaces. Various practical applications of stimuli-controlled hydrophilic–hydrophobic surfaces have been suggested such as self-cleaning surfaces,<sup>[16]</sup> sensors,<sup>[17]</sup> or delivery systems.<sup>[18]</sup> In a recent study,<sup>[19]</sup> we reported on the electroswitchable hydrophilic–hydrophobic properties of a Ag<sup>+</sup>-thiolated monolayer associated with a Au electrode. We demonstrated that the electrogenerated Ag<sup>0</sup> nanoclusters formed on the thiolated monolayer exhibit enhanced hydrophilicity as compared to the Ag<sup>+</sup>-thiolated monolayer.

In the present study we report on the formation of Hg<sup>2+</sup>-coated densely packed monolayers of aromatic dithiol on Au evaporated on a glass substrate, and on the reversible electrochemical control of the surface properties by the potential-induced cyclic generation and dissolution of Hg<sup>0</sup> nanoclusters.

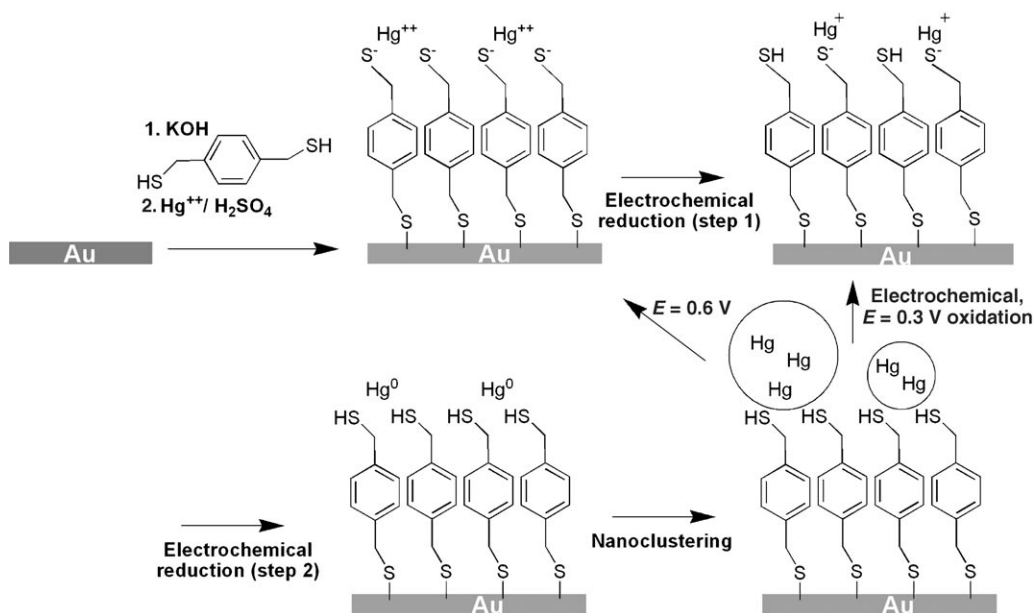
## Results and Discussion

1,4-Benzenedimethanethiol (BDMT) was oxidatively deposited on a Au electrode by using linear-sweep voltammetry in a basic solution of BDMT.<sup>[20]</sup> According to the coulometric analysis of the anodic deposition peak obtained upon the binding of BDMT on the Au surface (see Figure S1 in the Supporting Information), and assuming a one-electron oxidative adsorption of the dithiol [Eq. (1)], the surface coverage of the BDMT monolayer was estimated to be (0.52 ± 0.1) nmole cm<sup>-2</sup>. This value translates to a 32 Å<sup>2</sup>-footprint of BDMT, that is close to the coverage of a densely packed, vertically oriented, BDMT monolayer.<sup>[20a]</sup> The resulting monolayer was then treated with Hg<sup>2+</sup> ions to form the Hg<sup>2+</sup>-thiolated monolayer (Scheme 1). The generated surface was then rinsed to remove any nonspecifically adsorbed

mercury ions. Further studies were performed on the Hg<sup>2+</sup>-functionalized monolayer electrode in the absence of Hg<sup>2+</sup> ions in the bulk solution.



The Hg<sup>2+</sup>-functionalized monolayer electrode reveals two quasi-reversible redox processes at  $E_{1/2}^1 = 0.48$  V and  $E_{1/2}^2 = 0.20$  V (at the potential scan rate of 20 mVs<sup>-1</sup>) corresponding to the transformation of the monolayer from the Hg<sup>2+</sup> to the Hg<sup>+</sup> state and from the Hg<sup>+</sup> to the Hg<sup>0</sup> state, respectively (Figure 1A and 1B). The coulometric analysis of the corresponding waves in the cyclic voltammograms indicates a surface coverage of approximately (0.26 ± 0.2) nmole cm<sup>-2</sup>. Thus, the ratio of Hg<sup>2+</sup> ions and the supporting dithiol linkers is about 1:2, as depicted in Scheme 1. The cyclic voltammograms shown in Figure 1A and 1B are reproducible upon the application of many cycles of the potential, implying that the mercury species in different oxidation states are strongly bound to the supporting dithiol monolayer on the electrode surface. The cyclic voltammograms corresponding to both redox transformations of the monolayer demonstrate linear dependence of the peak currents versus the potential scan rate (Figure 1A and 1B, insets), thus indicating, as expected, that the electrochemical processes correspond to the surface-confined mercury cations associated with the dithiol monolayer. The quasi-reversible character of the redox processes was characterized by following the shifts of the peak potentials in the cyclic voltammograms upon increasing the potential scan rates (see Figure S2A and S2B in the Supporting Information). The cathodic and anodic peaks in the cyclic voltammograms depicted in Figure 1A and 1B



Scheme 1. Assembly of the Hg<sup>2+</sup>-dithiol monolayer-functionalized electrode and the reversible electrochemical generation of the Hg<sup>0</sup> nanoclusters associated with the modified interface.

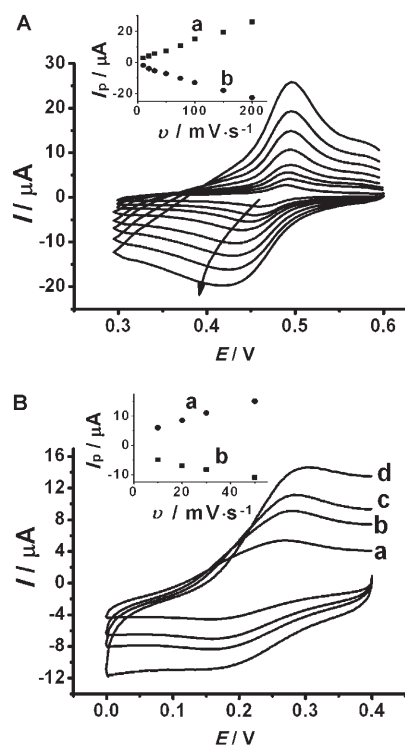


Figure 1. A) Cyclic voltammograms of the  $\text{Hg}^{2+}/\text{BDMT}/\text{Au}$  electrode recorded at different potential scan rates: 10, 20, 30, 50, 75, 100, 150, 200  $\text{mV s}^{-1}$ , with respect to the arrow direction. Inset: Dependence of the anodic (a) and cathodic (b) peak currents of the cyclic voltammograms on the potential scan rate. B) Cyclic voltammograms of the  $\text{Hg}^{2+}/\text{BDMT}/\text{Au}$  electrode recorded at different potential scan rates, after holding it under potential of 0.3 V for 10 min: a) 10  $\text{mV s}^{-1}$ ; b) 20  $\text{mV s}^{-1}$ ; c) 30  $\text{mV s}^{-1}$ ; d) 50  $\text{mV s}^{-1}$ . Inset: Dependence of the anodic (a) and the cathodic (b) peak currents of the cyclic voltammograms on the potential scan rate. The experiments were performed in 0.1 M  $\text{H}_2\text{SO}_4$  under an Ar atmosphere.

are shifted differently upon increasing the potential scan rate, thus resulting in a minor discrepancy between the middle point potentials,  $E_{1/2}$ , and the thermodynamic redox potentials,  $E^0$ , for both redox transformations. For potential scan rates lower than 20  $\text{mV s}^{-1}$ , the  $E_{1/2}$  values derived from the cyclic voltammograms can be approximated, however, as the  $E^0$  values of the redox transformations (ca. 0.48 and 0.20 V for the  $\text{Hg}^{2+}/\text{Hg}^+$  and  $\text{Hg}^+/\text{Hg}^0$  redox couples, respectively). The anodic and cathodic electron-transfer coefficients ( $\alpha$  and  $\beta$ , respectively) for both redox processes were derived from the slopes of  $E_{\text{peak}}/\log(\text{potential scan rate})$  dependence (see Figure S2A and S2B in the Supporting Information) resulting in a ratio of  $\alpha/\beta$  of about 4:1 for the  $\text{Hg}^{2+}/\text{Hg}^+$  redox process and a value of about 3:5 for the  $\text{Hg}^+/\text{Hg}^0$  redox couple. The derived difference in the anodic and cathodic electron-transfer coefficients still allows the application of the Laviron theory for the rough estimation of the electron-transfer rate constants,  $k_{\text{et}}$ , to be approximately 20 and 8  $\text{s}^{-1}$  for the  $\text{Hg}^{2+}/\text{Hg}^+$  and  $\text{Hg}^+/\text{Hg}^0$  surface-confined redox transformations, respectively.<sup>[21]</sup>

Further characterization of the electrochemical kinetics of the redox transformations of the mercury species associated with the supporting dithiol monolayer was obtained by chronoamperometric measurements.

The anodic (curves a) and cathodic (curves b) current transients corresponding to the oxidation and the reduction of the mercury-functionalized monolayer for the  $\text{Hg}^{2+}/\text{Hg}^+$  and  $\text{Hg}^+/\text{Hg}^0$  redox transformations are depicted in Figure 2A and 2B, respectively. The

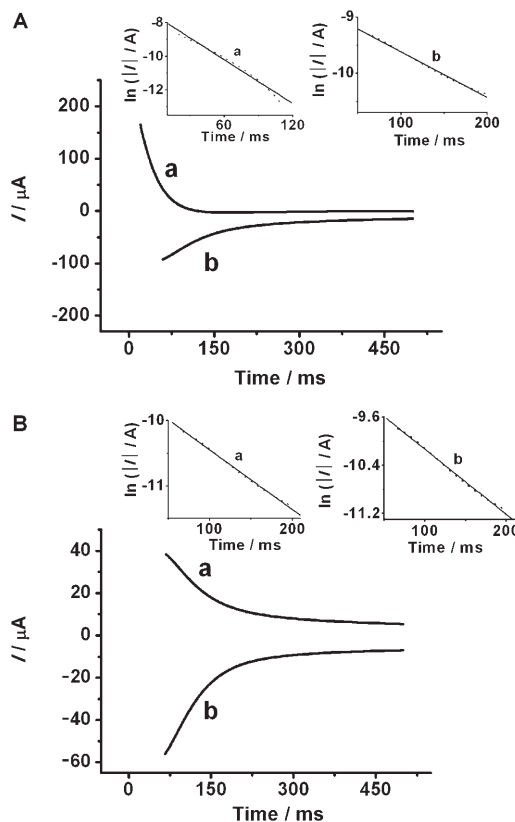


Figure 2. A) Chronoamperometric transients measured on the  $\text{Hg}^{2+}/\text{BDMT}/\text{Au}$  electrode upon the potential steps: a) from 0.3 to 0.6 V; b) from 0.6 to 0.3 V. Insets: Linearization of the respective current transients in semilogarithmic coordinates: a) of the anodic transient; b) of the cathodic transient. B) Chronoamperometric transients measured on the  $\text{Hg}^+/\text{BDMT}/\text{Au}$  electrode upon the potential steps: a) from 0 to 0.3 V; b) from 0.3 to 0 V. Insets: Linearization of the respective current transients in semilogarithmic coordinates: a) of the anodic transient; b) of the cathodic transient. The experiments were performed in 0.1 M  $\text{H}_2\text{SO}_4$  under an Ar atmosphere.

experimental current transients shown in Figure 2A and 2B were replotted in semilogarithmic coordinates (the respective insets), and these show linear dependence with time, thus demonstrating monoexponential current decays for all redox systems. The monoexponential character of the current transients provides evidence for the homogeneous structures of the redox monolayers.<sup>[22]</sup> The current transients,  $I(t)$ , were analyzed according to Equation [2], where  $k_{\text{et}}$  corresponds to the interfacial electron transfer and  $Q$  corresponds to the charge associated with the respective redox process of the surface-confined species.<sup>[22]</sup>

$$I(t) = k_{\text{et}}Q \exp(-k_{\text{et}}t) \quad (2)$$

The derived  $Q$  values, corresponding to the charges associated with the redox transformations of the respective electroactive species, are similar to those calculated by the integration of the respective waves in the cyclic voltammograms, thus resulting in the same surface coverage of the mercury species on the dithiol monolayer (ca.  $(0.26 \pm 0.2)$  nmole  $\text{cm}^{-2}$ ). The rate constants,  $k_{\text{et}}$ , derived from the chronoamperometric measurements (Table 1) are in good

Table 1. Electron-transfer rate constant,  $k_{\text{et}}$ , derived from the chronoamperometric measurements.

	Oxidation process [ $\text{s}^{-1}$ ]	Reduction process [ $\text{s}^{-1}$ ]	Average value [ $\text{s}^{-1}$ ] (The Laviron value [ $\text{s}^{-1}$ ])
$\text{Hg}^{2+}/\text{Hg}^+$ redox pair	43	8	25.5 (20)
$\text{Hg}^+/\text{Hg}^0$ redox pair	9	11	10 (8)

agreement with the rate constants roughly evaluated for the respective processes by the Laviron theory. The different rate constants for the anodic and cathodic processes derived from the chronoamperometric measurements are consistent with the nonsymmetrical shifts of the anodic and cathodic peaks in the cyclic voltammetry measurements upon increasing the potential scan rates.

The reduction of the  $\text{Hg}^{2+}$ -thiolated monolayer to the  $\text{Hg}^0$ -thiolated monolayer and the formation of  $\text{Hg}^0$  nanoclusters was characterized by scanning electron microscopy (SEM) imaging. Figure 3A shows the SEM image of the  $\text{Hg}^{2+}$ -BDMT monolayer-functionalized Au electrode, and this is compared to the SEM image obtained after the reduction of the surface-confined mercury ions to the  $\text{Hg}^0$ -BDMT state (Figure 3B). One can see that the electrochemical reduction of the  $\text{Hg}^{2+}$ -modified Au electrode results in the formation of  $\text{Hg}^0$  nanoclusters. The sizes of the bright-edged objects attributed to  $\text{Hg}^0$  nanoclusters range from 30 nm to 2  $\mu\text{m}$  (Figure 3B and Figure S3 in the Supporting Information). The formation of these patterns is fully reversible, that is, oxidation of the  $\text{Hg}^0$ -modified electrode to  $\text{Hg}^{2+}$ -modified surface, regenerates the SEM image shown in Figure 3A. The chemical composition of the surfaces at the different oxidation states was elucidated by energy-dispersive spectroscopy (EDS) measurements. The EDS spectrum of the  $\text{Hg}^{2+}$ -functionalized electrode surface (upon application of the potential of 0.6 V on the electrode) shows homogeneous distribution of  $\text{Hg}^{2+}$  ions on the surface. On the other hand, the reduced  $\text{Hg}^0$ -functionalized surface (generated upon the application of 0 V on the electrode) reveals different compositions that depend on the positioning of the electron beam on the surface. Focusing the electron beam on the bright patterns (Figure 3B) indicates the spectral signal characteristic to mercury (75–89% of mercury), whereas targeting the beam between the  $\text{Hg}^0$  clusters indicates areas that completely lack mercury (0% of mercury).

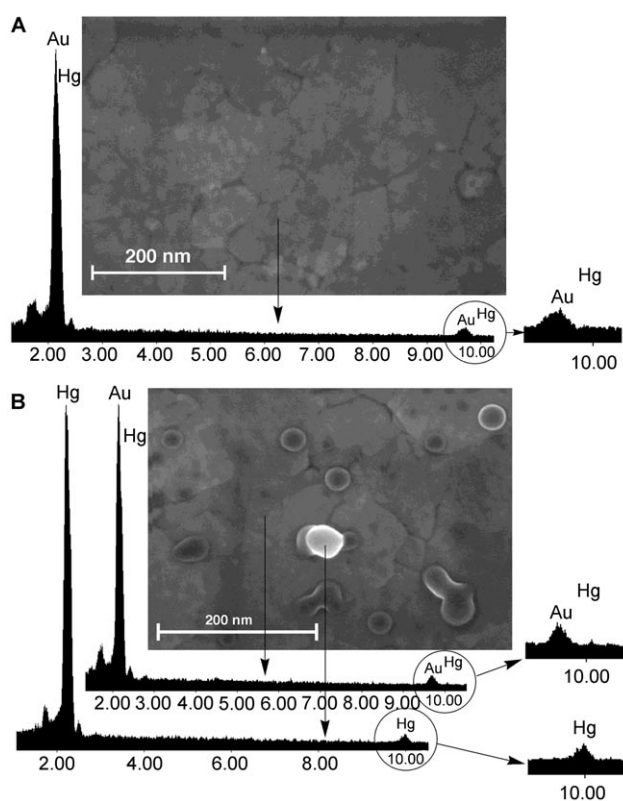


Figure 3. A) SEM image of the  $\text{Hg}^{2+}$ /BDMT-functionalized Au surface, generated by the application of a potential of 0.6 V for 10 min, with the corresponding EDS spectrum of the  $\text{Hg}^{2+}$ /BDMT-functionalized Au surface. B) SEM image of the  $\text{Hg}^0$ /BDMT-functionalized Au surface, generated by the application of a potential of 0 V for 10 min, with the corresponding EDS spectra of the  $\text{Hg}^0$ /BDMT-functionalized Au surface upon focusing the electron beam on a bright-edged domain or on an interdomain area of the SEM image.

To further understand the electrochemically induced transitions of mercury ions to  $\text{Hg}^0$  metal clusters and back, we applied in situ electrochemical surface plasmon resonance (SPR) measurements. The coupling of the localized plasmon of conductive metal nanoparticles ( $\text{Hg}^0$ ) with the surface plasmon of metal (Au) support is known to significantly affect the surface plasmon resonance spectrum, and to induce a significant shift in the minimum reflectivity angle.<sup>[23]</sup> This physical effect was extensively used to amplify biorecognition events<sup>[24]</sup> and biocatalytic transformations<sup>[25]</sup> by using Au or Ag nanoparticles as labels. Thus, the formation of  $\text{Hg}^0$  nanoclusters on the monolayer-modified Au electrode is anticipated to result in the electron coupling between the  $\text{Hg}^0$  plasmon and the Au surface plasmon wave and, consequently, to affect the resonance features of the SPR spectrum. The electrochemically induced transition of the  $\text{Hg}^{2+}$ -functionalized surface to the  $\text{Hg}^+$ -functionalized surface, upon stepping the potential from 0.6 to 0.3 V, does not result in any significant change in the SPR spectrum (see Figure S4 in the Supporting Information). Figure 4A depicts the time-dependent SPR spectra upon applying a potential step from  $E=0.3$  to  $E=0$  V on the  $\text{Hg}^+$ -functionalized monolayer. At the latter potential, the  $\text{Hg}^+$  ions are re-

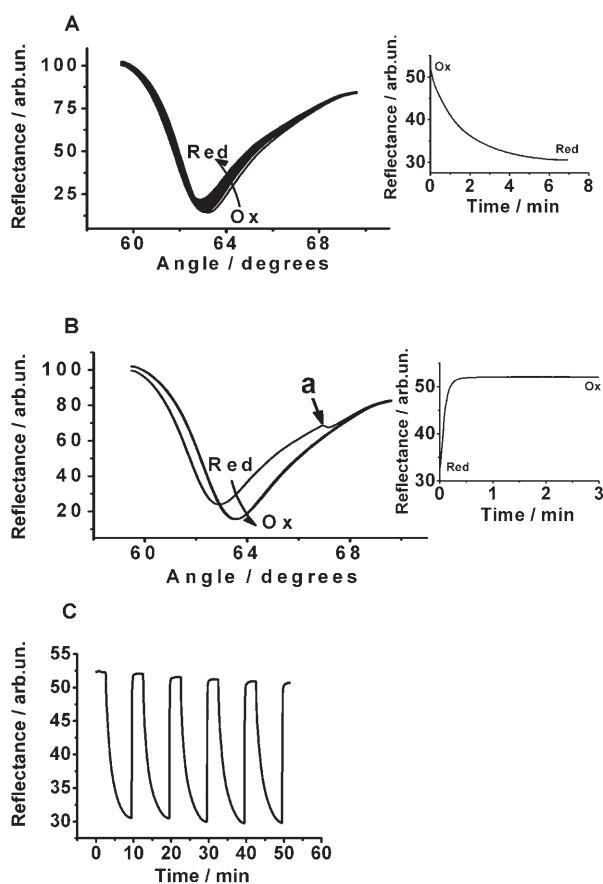


Figure 4. A) Time-dependent SPR spectra of the  $\text{Hg}^{+0}/\text{BDMT}/\text{Au}$  system after applying a potential step from 0.3 to 0 V. Inset: Change of the reflectance of the modified electrode measured at a constant angle of  $62.0^\circ$  upon the potential step from 0.3 to 0 V. B) Time-dependent SPR spectra of the  $\text{Hg}^{+0}/\text{BDMT}/\text{Au}$  system after applying a potential step from 0 to 0.3 V. Inset: Change of the reflectance of the modified electrode measured at a constant angle of  $62.0^\circ$  upon the potential step from 0.3 to 0 V. Point **a** shows the timing of oxidative potential step application on the  $\text{Hg}^0$ -modified electrode. C) Reversible changes of the reflectance of the  $\text{Hg}^{+0}/\text{BDMT}/\text{Au}$  system at a constant angle of  $62.0^\circ$  upon cyclic application of 0.3 and 0 V on the modified electrode. The experiments were performed in 0.1 M  $\text{H}_2\text{SO}_4$  under an Ar atmosphere. Red: represents the system in the reduced state containing  $\text{Hg}^0$  nanoclusters; Ox: represents the system in the oxidized state containing  $\text{Hg}^+$  ion redox species.

duced to the  $\text{Hg}^0$  nanoclusters. The formation of the  $\text{Hg}^0$  nanoclusters is accompanied by a shift of the minimum reflectivity angles to lower values and the formation of a shallower SPR curve. The change in the SPR spectrum can be explained by the coupling of the localized plasmons of the nanoclusters with the surface plasmon of the Au support. Similar changes were observed in the SPR spectra upon the reduction of the other metal ions to metal nanoclusters.<sup>[26]</sup> Figure 4A, inset, shows the time-dependent changes in the reflectance at a constant angle of  $62.0^\circ$ . The changes in the SPR spectra proceed for about five minutes, and then level off to a constant reflectance value. Interestingly, the time scale of chemical transformation occurring on the surface, and being probed by the SPR spectra, is approximately three orders of magnitude lower than the electron transfer

to  $\text{Hg}^+$  that yields  $\text{Hg}^0$  (ca. 200 ms, as elucidated by the chronoamperometric experiments, Figure 3A). This apparent discrepancy may be resolved by realizing that the chronoamperometric measurements follow the fast electron-transfer process, whereas the SPR spectroscopy follows the secondary slow process of the cluster formation. The migration of the  $\text{Hg}^0$  atoms on the surface and their clustering into metal islands is a substantially slower process compared to the primary electron-transfer step. Since the SPR spectra follow the phenomenon of coupling between the localized plasmon of the nanoclusters and the Au-surface plasmon, the kinetics of  $\text{Hg}^0$  declustering is monitored optically. The electrochemically induced transition from the  $\text{Hg}^0$  state to the  $\text{Hg}^+$  state, upon the potential step from 0 to 0.3 V, results in the fast regeneration of the SPR spectrum characteristic of the  $\text{Hg}^+$  state (Figure 4B). The major time-dependent changes in the SPR spectra proceed within 15 s (Figure 4B, inset). This time interval is still substantially longer than the related electron-transfer step followed by chronoamperometry (Figure 2B). The time scale required to stabilize the SPR spectra of the electrochemically generated  $\text{Hg}^+$  monolayer is attributed to the migration of the  $\text{Hg}^+$  ions on the surface upon dissolution of the  $\text{Hg}^0$  nanoclusters to form the stable  $\text{Hg}^+$ -thiolated monolayer surface. Figure 4C shows the cyclic changes of the reflectance intensities (at ca.  $62.0^\circ$ ) upon the reversible switching of the monolayer configuration between the  $\text{Hg}^0$  nanocluster and  $\text{Hg}^+$  ion states, respectively. It should be noted that the alternate application of the potential values of 0.6, 0.3, and 0 V on the BDMT monolayer-functionalized Au electrode in the absence of the  $\text{Hg}^{2+}/\text{Hg}^+/\text{Hg}^0$  surface-confined redox system yields only a minute change in the minimum reflectivity angle, as well as in the reflectance intensities. Thus, the observed changes in the SPR spectra originate from the reversible formation of the  $\text{Hg}^0$  nanoclusters and their dissolution upon reductive and oxidative potential steps, respectively.

The monolayer-functionalized electrode was further characterized by means of X-ray photoelectron spectroscopy (XPS).<sup>[27]</sup> The goal of the XPS measurements was to estimate and identify the chemical states of mercury on the BDMT monolayer upon application of the potentials corresponding to the three different oxidation states of mercury, and to estimate the molar ratio of the surface-confined mercury to the dithiol molecules in the supporting monolayer. Figure 5A and 5B show the XPS spectra of carbon (1s) and sulfur (2p) core levels, respectively. Figure 5C shows spectra of the Hg 4f doublet for: a)  $\text{Hg}^0$ -BDMT-, b)  $\text{Hg}^+$ -BDMT-, c)  $\text{Hg}^{2+}$ -BDMT-functionalized surfaces at a grazing emission angle of  $70^\circ$  (with respect to the surface normal), obtained after holding the system under the corresponding potentials of a) 0, b) 0.3, and c) 0.6 V in a solution of  $\text{H}_2\text{SO}_4$  (0.1 M), over a period of 10 min. The samples were installed under ultra-high-vacuum conditions only after 2 h, and hence a partial oxidation of the  $\text{Hg}^0$  nanoclusters can be assumed. Deconvolution of the emission lines suggests the major presence of the reduced  $\text{Hg}^0$  form (ca. 60%) in (a), according to the peak position (100.1 eV), characteristic for

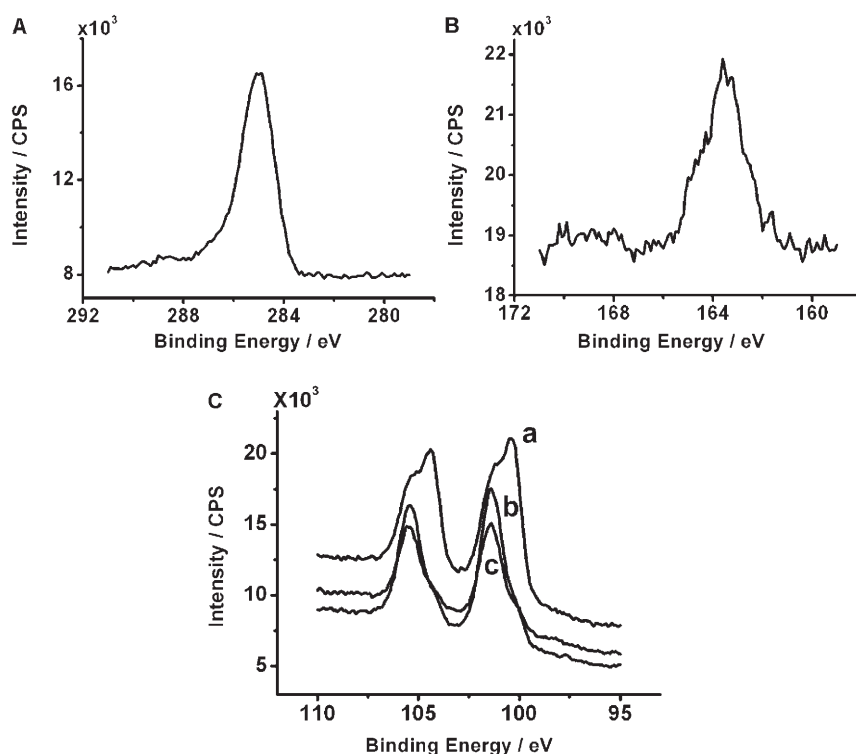


Figure 5. High-resolution XPS spectra of: A) carbon (1s); B) sulfur (2p), core levels from  $\text{Hg}^{2+}$ -BDMT monolayer-functionalized Au surface (held under the potential of 0.6 V for 10 min) at normal electron emission angle ( $0^\circ$ ). The ratio of atomic concentrations of the sulfur (163.6 eV) and carbon (285.0 eV) signals confirms the presence of the BDMT monolayer on the Au surface. C) High-resolution spectra of the Hg 4f doublet for: a)  $\text{Hg}^0$ /BDMT/Au; b)  $\text{Hg}^+$ /BDMT/Au; c)  $\text{Hg}^{2+}$ /BDMT/Au interfaces, generated by the application of constant potentials of: 0, 0.3 and 0.6 V, respectively, for 10 min at grazing electron emission angle ( $70^\circ$ ). CPS = counts per second.

atomic mercury. The (b) and (c) spectra show almost completely (above 90%) oxidized  $\text{Hg}^+$  and/or  $\text{Hg}^{2+}$  species present on the interface, giving a binding energy shift of 101.5 eV. Unfortunately, the oxidized states of mercury ( $\text{Hg}^{2+}$  and  $\text{Hg}^+$ ) cannot be distinguished by the XPS technique. Elemental quantification in terms of the atomic concentration ratio ( $\text{Hg}(4f)/\text{S}(2p)/\text{C}(1s)$ ) derived by integration of the corresponding peaks results in the mercury/BDMT ratio of about 1:2, a value that nicely correlates with the result derived from the electrochemical measurements.

Various approaches for controlling the hydrophobic-hydrophilic properties of surfaces were discussed,<sup>[1]</sup> including the preparation of rough surfaces coated with hydrophobic materials or the fabrication of ordered microstructured surfaces. The cyclic electrochemical switching of the  $\text{Hg}^{2+}$ -BDMT-coated surface to the  $\text{Hg}^+$ - and to  $\text{Hg}^0$ -nanocluster-modified interface suggests that the hydrophilic-hydrophobic properties of the surface could be electrochemically controlled upon undergoing the cyclic transition of  $\text{Hg}^{2+}$  to  $\text{Hg}^+$  and to  $\text{Hg}^0$ . Figure 6 shows the in situ electrochemically controlled contact-angle changes of a droplet of  $\text{H}_2\text{SO}_4$  (0.1 M) upon cyclic switching of the potential on the electrode between 0.6, 0.3, and 0 V, corresponding to the three oxidation states of the mercury-BDMT interface, respectively. The droplet was equilibrated with the modified interface

on the time scale of the experiment, and the derived contact angles reflected the equilibrium corresponding to the potential-controlled redox state of the modified surface. At an applied potential of 0.6 V, where the BDMT surface is functionalized with the  $\text{Hg}^{2+}$  ions, the contact angle has a value in the region of  $(64 \pm 3)^\circ$ . At an applied potential of 0.3 V, where the  $\text{Hg}^+$  ions are linked to the monolayer interface, a somewhat lower contact angle, corresponding to  $(57 \pm 1)^\circ$  is observed. On the other hand, stepping the potential further to 0 V caused a sharp increase in the hydrophobicity of the surface, and the resulting advancing contact angle of about  $(76 \pm 1)^\circ$ . In a control experiment where the potential was cycled on the BDMT-modified electrode that lacks any mercury ions, between the values of 0 and 0.6 V, only minute changes of approximately  $1.5^\circ$  in the contact angle of the  $\text{H}_2\text{SO}_4$  (0.1 M) droplet were observed. This

implies that the potential-induced contact-angle changes of the mercury-functionalized monolayer originate from the redox-stimulated reduction of the  $\text{Hg}^{2+}$  ions to  $\text{Hg}^+$  and to  $\text{Hg}^0$  nanoclusters, and the reverse dissolution of the nanoparticles, respectively. The  $\text{Hg}^0$ -nanocluster-modified interface reveals hydrophobic properties, whereas the  $\text{Hg}^{2+}$ - and especially the  $\text{Hg}^+$ -thiolated monolayer interfaces exhibit hydrophilic properties based on the contact-angle measurements. It should be noted that the ion-free BDMT-function-

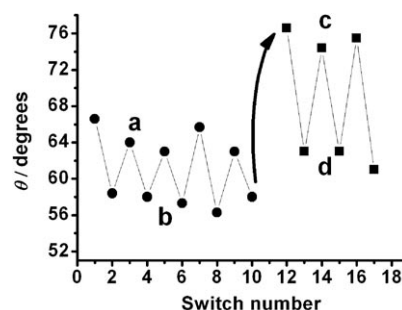


Figure 6. Reversible in situ changes of the contact angle of a 0.1 M  $\text{H}_2\text{SO}_4$  aqueous droplet on the  $\text{Hg}^{2+}/\text{BDMT}/\text{Au}$  system upon application of the potentials: a) 0.6; b) 0.3; c) 0; d) 0.6 V. At each point the measurement was performed after holding the system under the corresponding potential for 5 min.

alized Au surface exhibits a clear hydrophobic contact angle of about  $80^\circ$ , very weakly dependent on the applied potential. This value corresponds with the contact-angle values of densely packed monolayers of aromatic dithiols reported in the literature.<sup>[28]</sup>

Further confirmation of the control of the hydrophilicity–hydrophobicity of the interface by the redox transformations driven through the three electroactive species,  $\text{Hg}^0$ ,  $\text{Hg}^+$ , and  $\text{Hg}^{2+}$ , was obtained through AFM force measurements. In these experiments the affinity between a hydrophobically modified AFM tip and the modified surface in the different oxidation states was monitored in solution. The force curves were recorded on four different  $5 \times 5 \mu\text{m}^2$  sample spots, yielding a total number of approximately 900 measured force values for each oxidation state. Figure 7 shows the cor-

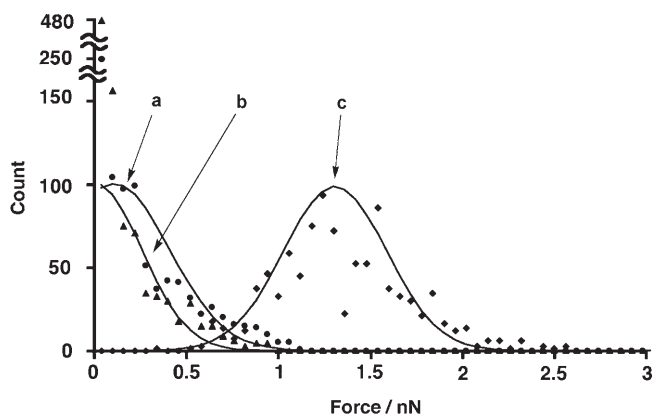


Figure 7. Distribution of the measured pull-off forces between a hydrophobic AFM tip and the modified surfaces in different oxidation states: a)  $\text{Hg}^{2+}$ ; b)  $\text{Hg}^+$ ; c)  $\text{Hg}^0$ . The data points represent the frequency of a specific pull-off force, the solid lines represent the Gaussian fits to the data. The measurements were performed in a solution of  $\text{Na}_2\text{SO}_4$  (0.1 M) at pH 3.

responding force distribution for these measurements. The results clearly show a strong interaction between the hydrophobic tip and the  $\text{Hg}^0$ -modified surface, exhibiting an average force of approximately 1.3 nN. This is attributed to the hydrophobic interaction between the tip and the sample in the aqueous environment. The two different oxidized states of Hg reveal much lower forces, reaching the limit of sensitivity of our AFM setup for hydrophobic interactions, indicating a higher hydrophilicity as compared to the  $\text{Hg}^0$  interface. The Gaussian fits were normalized to the number of force curves measured, yielding values of approximately 0.1 nN for  $\text{Hg}^{2+}$  and  $-0.1$  nN for  $\text{Hg}^+$ . It should be noted, that the Gaussian distribution does not seem to fit the forces below 0.06 nN (leftmost point in the graph) but it needs to be kept in mind that these data points are the sum of all measurements exhibiting an interaction that is lower than the sensitivity of the instrument towards hydrophobicity and, therefore, comprise the complete second half of the Gaussian curve. It was possible to switch, reversibly, between the characteristic force values of each of the three

systems by converting the oxidation state of the surface-bound Hg between  $\text{Hg}^0$ ,  $\text{Hg}^+$ , and  $\text{Hg}^{2+}$ .

## Conclusion

The present study has examined the electrochemical transformation of a  $\text{Hg}^{2+}$ -functionalized thiolated monolayer into  $\text{Hg}^0$  nanoclusters bound to the thiolated monolayer, and the dissolution of the  $\text{Hg}^0$  nanoclusters to the  $\text{Hg}^{2+}$ -modified thiolated monolayer. The formation of the  $\text{Hg}^0$  nanoclusters involves the rapid reduction of  $\text{Hg}^{2+}$  to  $\text{Hg}^+$ ,  $8 \text{ s}^{-1}$ , and of  $\text{Hg}^+$  to  $\text{Hg}^0$  atoms,  $11 \text{ s}^{-1}$ , followed by the slow clustering of the  $\text{Hg}^0$  atoms on the surface (a process that proceeds for minutes). The  $\text{Hg}^0$  nanoclusters have dimensions in the range of 30 nm to  $2 \mu\text{m}$ . Formation of the nanoclusters and their dissolution were characterized by electrochemical methods, SPR, SEM, XPS, and contact-angle measurements. The dissolution of the nanoclusters through oxidation of the  $\text{Hg}^0$  nanoclusters proceeds through a rapid electron transfer to form  $\text{Hg}^+$  and  $\text{Hg}^{2+}$ , 9 and  $43 \text{ s}^{-1}$ , respectively, followed by a slower surface redistribution of the ions (a process that proceeds at around 15 s). The  $\text{Hg}^0$ -nanoclustered surface reveals enhanced hydrophobicity as compared to the  $\text{Hg}^+$ -thiolated monolayer, contact angle  $76^\circ$  as compared to  $57^\circ$ , respectively. One important conclusion of the study is that the  $\text{Hg}^0$  nanoclusters and the dissolved  $\text{Hg}^{2+}$  ions form a stable intact structure with the thiolated monolayer, without the dissolution of mercury species to the electrolyte solution. These results, together with our related observation on the formation of  $\text{Ag}^0$  nanoclusters and their dissolution on a thiolated monolayer,<sup>[19]</sup> suggest that nanoclusters of other metals could be deposited on electrodes. Such functionalized electrodes might find important applications as electrocatalytic electrodes for fuel cells or electrosynthesis.

## Experimental Section

**Chemicals:** 1,4-Benzenedimethanethiol (BDMT) and other chemicals were purchased from Aldrich and used as supplied. Ultrapure water from a NANOpure Diamond (Barnstead) source was used throughout all the experiments.

**Modification of electrodes:** A Au-coated (50 nm gold layer) glass plate ( $22 \times 22 \text{ mm}^2$ ) (Analytical  $\mu$ -Systems, Germany) was used as a working electrode. Prior to the modification, the Au surface was flame-annealed for 5 min in a *n*-butane flame and cooled for 10 min under a weak stream of Ar gas. The BDMT monolayer was electrochemically oxidatively deposited on a Au electrode according to the following procedure.<sup>[20]</sup> A Au electrode was immersed into a solution of BDMT (1 mM) in KOH (0.5 M) under an Ar atmosphere and preconditioned at  $-1.0 \text{ V}$  for 10 min to obtain a thiol-free Au surface. The applied potential was then swept to  $-0.65 \text{ V}$  with the potential scan rate of  $20 \text{ mV s}^{-1}$  and the potential was held for 1 min at  $-0.65 \text{ V}$ , resulting in the oxidative anodic deposition of the BDMT self-assembled monolayer (see Figure S1 in the Supporting Information). The BDMT-modified electrode was thoroughly rinsed with water and soaked in a solution of  $\text{HgCl}_2$  (10 mM) in  $\text{H}_2\text{SO}_4$  (0.1 M) overnight to yield the  $\text{Hg}^{2+}$ -dithiol complex on the Au surface.

**Electrochemical, contact angle, surface plasmon resonance (SPR), energy-dispersive spectroscopy (EDS), scanning electron microscopy**

(SEM), X-ray photoelectron spectroscopy (XPS), and atomic force microscopy (AFM) measurements: The cyclic and linear-sweep voltammetry as well as in situ measurements under constant potential applied on the modified electrode were performed by using an electrochemical PC-controlled analyzer-potentiostat IVIUM (PalmSensPC software). The chronoamperometric measurements were performed on an electrochemical analyzer Potentiostat/Galvanostat (EG&G Model 283) connected to a computer (EG&G Software No 270/250). In situ electrochemical measurements coupled with static contact-angle measurements were performed on the modified Au-coated glass plates by using a CAM2000 optical-angle analyzer (KSV Instruments, Finland), and the PalmSense potentiostat. An aqueous droplet of approximately 20  $\mu\text{L}$  of  $\text{H}_2\text{SO}_4$  (0.1 M) with the controlled diameter of the footprint of 0.5 cm was deposited from a syringe onto the modified surface (wired as a working electrode). Then the counter-electrode wire (Pt wire with a diameter of 0.1 mm) and the quasi-reference electrode (Ag wire with a diameter of 0.1 mm) were introduced into the droplet. All the potentials were reported versus the silver-wire quasi-reference electrode, calibrated according to the relation:  $E_{\text{Ag}/\text{AgCl}(\text{KCl},\text{sat})} + 0.11 \text{ V} = E_{\text{Ag wire}}$ . Prior to contact-angle measurement the droplet was kept under the applied potential for 5 min to allow it to achieve the equilibrium shape. The images of the droplets were recorded and each contact-angle value was measured at least six times, and the derived average contact-angle values had a precision of  $\pm 0.1^\circ$ . The  $\text{Hg}^{2+}/\text{BDMT}/\text{Au}$  or  $\text{Hg}^0/\text{BDMT}/\text{Au}$  system was electrochemically reduced to generate  $\text{Hg}^0$  nanoclusters associated with the modified surface and was then oxidized back to the  $\text{Hg}^{2+}$  or  $\text{Hg}^+$  ionic state. These electrochemical processes were performed in the droplet upon measuring in situ the contact angles.

The XPS spectra were measured on the XPS device, model Kratos Axis Ultra, supplied with an  $\text{Al}_{\text{K}\alpha}$ -monochromated source ( $h\nu = 1486.6 \text{ eV}$ , 150–225 W). The spectra (experimental resolution of less than 0.5 eV) were measured at normal emission, by using the passing energy of the analyzer of 40 eV. The measurements were performed under conditions of UHV (ultrahigh vacuum). Before the peak fitting of the background noise was subtracted by the Shirley system. Two angles for high-resolution measurements were used:  $0^\circ$  (normal) and  $70^\circ$  (grazing).

The SPR Kretschmann-type spectrometer "BIOSUPLAR-2" (light-emitting diode light source  $\lambda = 670 \text{ nm}$ ) and the Au-covered glass slides (1.5  $\text{cm}^2$  area exposed to the solution) from Analytical  $\mu$ -Systems (Germany) were used in this work. An auxiliary Pt and a quasireference Ag electrode made from wires of 0.5 mm diameter were parts of the cell, thus allowing in situ electrochemical SPR measurements upon the electrochemical processes on the modified surface.

AFM measurements were performed with a SMENA-B atomic force microscope (NT-MDT, Russia) equipped with a SMENA-A scanner head. Silicon cantilevers (CSC12, MikroMasch, Russia) with a nominal spring constant of 0.03 were cleaned in a UV/ozone (T10 $\times$ 10, UVOCs Inc.) chamber for 10 min and were modified with octadecyltrichlorosilane (OTS) by immersion into a 1% solution of OTS in toluene for 2 min, followed by subsequent rinsing with toluene, acetone, and ethanol, and blow drying with nitrogen. Samples were immersed into a solution of  $\text{Na}_2\text{SO}_4$  (0.1 M) at pH 3 for the determination of the force curves. Deflection–distance curves were measured for each substrate on four  $5 \times 5 \mu\text{m}^2$  sample spots, mapping the interaction between the tip and the sample on 225 points (15 $\times$ 15 data point mesh) on each of these areas. The obtained curves were exported as ASCII files and further processed by using MS Excel to extract the pull-off force for each individual curve.

The SEM measurements were performed on the respective modified Au-coated glass plates by using a UHR FEG SEM apparatus, model SIRION (FEI, USA), resolution 1.5 nm. The EDS analysis was performed on a Phoenix spectrometer (EDAX, USA), resolution 128 eV. Quantification of atomic percentages in EDS was done by the ZAF matrix-correction system.

## Acknowledgements

This study was supported by the German–Israeli Program (DIP) and by the Israel Science Foundation. We thank the Unit for Nanoscopic Characterization, The Hebrew University of Jerusalem for their help with these studies.

- [1] a) K. Kato, E. Uchida, E.-T. Kang, Y. Uyama, Y. Ikada, *Prog. Polym. Sci.* **2003**, *28*, 209–259; b) I. Luzinov, S. Minko, V. V. Tsukruk, *Prog. Polym. Sci.* **2004**, *29*, 635–698; c) Y. Liu, L. Mu, B. Liu, J. Kong, *Chem. Eur. J.* **2005**, *11*, 2622–2631.
- [2] X. Wang, A. B. Kharitonov, E. Katz, I. Willner, *Chem. Commun.* **2003**, 1542–1543.
- [3] a) T. Sun, G. Wang, L. Feng, B. Liu, Y. Ma, L. Jiang, D. Zhu, *Angew. Chem.* **2004**, *116*, 361–364; *Angew. Chem. Int. Ed.* **2004**, *43*, 357–360; b) Q. Fu, G. V. Rao, S. B. Basame, D. J. Keller, K. Artyushkova, J. E. Fulghum, G. P. Lopez, *J. Am. Chem. Soc.* **2004**, *126*, 8904–8905.
- [4] Z.-Z. Gu, A. Fujishima, O. Sato, *Angew. Chem.* **2002**, *114*, 2171–2174; *Angew. Chem. Int. Ed.* **2002**, *41*, 2067–2070.
- [5] F. Xia, L. Feng, S. Wang, T. Sun, W. Song, W. Jiang, L. Jiang, *Adv. Mater.* **2006**, *18*, 432–436.
- [6] X. Wang, E. Katz, I. Willner, *Electrochem. Commun.* **2003**, *5*, 814–818.
- [7] a) X. Wang, S. Zeevi, A. B. Kharitonov, E. Katz, I. Willner, *Phys. Chem. Chem. Phys.* **2003**, *5*, 4236–4241; b) R. Rosario, D. Gust, A. A. Garcia, M. Hayes, J. L. Taraci, T. Clement, J. W. Dailey, S. T. Picraux, *J. Phys. Chem. B* **2004**, *108*, 12640–12642; c) W. H. Jiang, G. J. Wang, Y. N. He, X. G. Wang, Y. L. An, Y. L. Song, L. Jiang, *Chem. Commun.* **2005**, 3550–3552.
- [8] E. Katz, L. Sheeney-Haj-Idia, B. Basnar, I. Felner, I. Willner, *Langmuir* **2004**, *20*, 9714–9719.
- [9] a) Y. G. Jiang, Z. Q. Wang, X. Yu, F. Shi, H. P. Xu, X. Zhang, *Langmuir* **2005**, *21*, 1986–1990; b) X. Yu, Z. Q. Wang, Y. G. Jiang, F. Shi, X. Zhang, *Adv. Mater.* **2005**, *17*, 1289–1293.
- [10] X. Wang, Z. Gershman, A. B. Kharitonov, E. Katz, I. Willner, *Langmuir* **2003**, *19*, 5413–5420.
- [11] J. Lahann, S. Mitragotri, T.-N. Tran, H. Kaido, J. Sundaram, I. S. Choi, S. Hoffer, G. A. Somorjai, R. Langer, *Science* **2003**, *299*, 371–374.
- [12] E. Katz, O. Lioubashevsky, I. Willner, *J. Am. Chem. Soc.* **2004**, *126*, 15520–15532.
- [13] K. Tadanaga, J. Morinaga, A. Matsuda, T. Minami, *Chem. Mater.* **2000**, *12*, 590–592.
- [14] a) Y.-H. Lin, J. Teng, E. R. Zubarev, H. Shulha, V. V. Tsukruk, *Nano Lett.* **2005**, *5*, 491–495; b) D. Juthongpiput, Y.-H. Lin, J. Teng, E. R. Zubarev, V. V. Tsukruk, *J. Am. Chem. Soc.* **2003**, *125*, 15912–15921.
- [15] a) S. Rifai, M. Lafferrière, D. Qu, D. D. M. Wayner, C. P. Wilde, M. Morin, *J. Electroanal. Chem.* **2002**, *531*, 111–118; b) S. Rifai, G. P. Lopinski, T. Ward, D. D. M. Wayner, M. Morin, *Langmuir* **2003**, *19*, 8916–8922.
- [16] a) R. Wang, K. Hashimoto, A. Fujishima, M. Chikuni, E. Kojima, A. Kitamura, M. Shimohigoshi, T. Watanabe, *Nature* **1997**, *388*, 431–432; b) X. J. Feng, L. Feng, M. H. Jin, J. Zhai, L. Jiang, D. B. Zhu, *J. Am. Chem. Soc.* **2004**, *126*, 62–63.
- [17] a) L. Liang, X. D. Feng, J. Liu, P. C. Rieke, *J. Appl. Polym. Sci.* **1999**, *72*, 1–11; b) L. Liang, X. D. Feng, J. Liu, P. C. Rieke, G. E. Fryxell, *Macromolecules* **1998**, *31*, 7845–7850; c) R. Gabai, N. Sallacan, V. Chegel, T. Bourenko, E. Katz, I. Willner, *J. Phys. Chem. B* **2001**, *105*, 8196–8202.
- [18] N. L. Abbott, G. M. Whitesides, *Langmuir* **1994**, *10*, 1493–1497.
- [19] M. Riskin, B. Basnar, V. I. Chegel, E. Katz, I. Willner, F. Shi, X. Zhang, *J. Am. Chem. Soc.* **2006**, *128*, 1253–1260.
- [20] a) S. Rifai, M. Lafferrière, D. Qu, D. D. M. Wayner, C. P. Wilde, M. Morin, *J. Electroanal. Chem.* **2002**, *531*, 111–118; b) S. Rifai, G. P. Lopinski, T. Ward, D. D. M. Wayner, M. Morin, *Langmuir* **2003**, *19*, 8916–8922.
- [21] E. Laviron, *J. Electroanal. Chem.* **1979**, *101*, 19–28.

- [22] a) R. J. Forster, L. R. Faulkner, *Anal. Chem.* **1995**, *67*, 1232–1239; b) R. J. Forster, *Langmuir* **1995**, *11*, 2247–2255; c) R. J. Forster, *Anal. Chem.* **1996**, *68*, 3143–3150; d) R. J. Forster, *Analyst* **1996**, *121*, 733–741; e) E. Katz, I. Willner, *Langmuir* **1997**, *13*, 3364–3373.
- [23] a) L. A. Lyon, M. D. Musick, P. C. Smith, B. D. Reiss, D. J. Pena, M. J. Natan, *Sens. Actuators B* **1999**, *54*, 118–124; b) L. A. Lyon, D. J. Pena, M. J. Natan, *J. Phys. Chem. B* **1999**, *103*, 5826–5831.
- [24] a) L. A. Lyon, M. D. Musick, M. J. Natan, *Anal. Chem.* **1998**, *70*, 5177–5183; b) L. He, M. D. Musick, S. R. Nicewarner, F. G. Sallinas, S. J. Benkovic, M. J. Natan, C. D. Keating, *J. Am. Chem. Soc.* **2000**, *122*, 9071–9077.
- [25] M. Zayats, S. P. Pogorelova, A. B. Kharitonov, O. Lioubashevski, E. Katz, I. Willner, *Chem. Eur. J.* **2003**, *9*, 6108–6114.
- [26] V. I. Chegel, O. A. Raitman, O. Lioubashevski, Y. Shirshov, E. Katz, I. Willner, *Adv. Mater.* **2002**, *14*, 1549–1553.
- [27] a) H.-T. Rong, S. Frey, Y.-J. Yang, M. Zharnikov, M. Buck, M. Wühn, C. Wöll, C. Helmchen, *Langmuir* **2001**, *17*, 1582–1593; b) F. P. Zamborini, J. K. Campbell, R. M. Crooks, *Langmuir* **1998**, *14*, 640–647; c) J. F. Kang, A. Ulman, S. Liao, R. Jordan, G. Yang, G.-Y. Liu, *Langmuir* **2001**, *17*, 95–106; d) C. Winter, U. Weckenmann, R. A. Fischer, J. Käshammer, V. Scheumann, S. Mittler, *Chem. Vap. Deposition* **2000**, *6*, 199–205.
- [28] B. De Boer, H. Meng, D. F. Perepichka, J. Zheng, M. M. Frank, Y. J. Chabal, Z. Bao, *Langmuir* **2003**, *19*, 4272–4284.

Received: February 27, 2006

Revised: May 18, 2006

Published online: August 17, 2006